13th International Symposium on Turbulence and Shear Flow Phenomena (TSFP13)
Montreal, Canada, June 25–28, 2024

THE AIRFLOW IN THE HUMAN NOSE: SIMULATIONS AND EXPERIMENTS OF CLINICAL INTEREST

Marco Atzori
Dipartimento di Scienze e Tecnologie Aerospaziali,
Politecnico di Milano,
via La Masa 34, 20156 Milano, Italy
marco.atzori@polimi.it

Guido Guglielmo Tesa
Dipartimento di Scienze e Tecnologie Aerospaziali,
Politecnico di Milano,
via La Masa 34, 20156 Milano, Italy
guidoguglielmo.tesa@mail.polimi.it

Gabriele Dini Ciacci
Dipartimento di Scienze e Tecnologie Aerospaziali,
Politecnico di Milano,
via La Masa 34, 20156 Milano, Italy
gab@diniciacci.org

Maurizio Quadrio
Dipartimento di Scienze e Tecnologie Aerospaziali,
Politecnico di Milano,
via La Masa 34, 20156 Milano, Italy
maurizio.quadrio@polimi.it

ABSTRACT

A computer code based on the immersed-boundary method (IBM) for direct numerical simulations (DNS) of the flow in the higher human airways is presented. It is shown that the IBM implementation fully preserves the spatial second-order discretization accuracy, so that it can be used for high-fidelity efficient simulations of the nasal cavity, allowing to describe the airflow and to evaluate the nasal resistance. Measurement of nasal resistance is a widely used clinical practice, but large discrepancies between computational fluid dynamic (CFD) and clinical measurements have been consistently reported. To identify the leading cause of the discrepancy, a comparison of nasal resistance from DNS, RANS simulations, and laboratory experiments is carried out. It is confirmed that the various uncertainties in simulations (deriving e.g. from the use of turbulence models) is way too low to explain the lack of agreement between clinical rhinomanometers and CFD. It is also found, for the specific device considered here, that the dominant cause of error in the clinical measurement is one of the locations where pressure is probed, as a consequence of the design of the device. This error is large enough to be compatible with the discrepancy reported in the literature.

INTRODUCTION

Studying the fluid mechanics of the human nose — *i.e.* the respiratory tract from the nostrils to the upper portion of the pharinxy — is motivated by the common occurrence of nasal airway obstructions (NAOs). Even though NAOs are not life-threatening conditions, they can cause severe discomfort and have a serious impact on life quality (Rhee *et al.*, 2003). Beyond symptom descriptions and the visual inspection of computed tomography (CT) scans, the nasal resistance is the main functional parameter that is considered for diagnoses and planning of surgeries. This quantity is defined as $R = \Delta P/Q$, where ΔP is the pressure drop during respiration between the outer ambient and the pharinxy, and Q is the corresponding flow rate. The resistance is clinically measured with an exam known as *rhinomanometry* (RMM) (Vogt *et al.*, 2010). While RMMs can be carried out with different approaches, the one considered the better compromise between accuracy and least invasiveness is the so-called Anterior Active Rhinomanometry (AAR), which will be described in details in the next section. Numerical simulations using geometries reconstructed from CT scans could also be used to estimate R and to provide a more complete description of the flow within the nasal cavity, as already done in a number of studies during the past two decades (Quadrio *et al.*, 2014; Radulesco *et al.*, 2019) and up to very recently (*e.g.* Calmet *et al.*, 2021; Schillaci *et al.*, 2024). Assuming these simulations are reliable enough, they could also be used to provide a more detailed description of the flow dynamics, and to enable data-driven methods (Schillaci *et al.*, 2022).

However, obtaining good agreement between RMM and CFD has proved to be challenging, with simulations significantly underestimating the nasal resistance (Kimbell *et al.*, 2012; Osman *et al.*, 2016). This remains true even in very recent studies. Berger *et al.* (2021), who carried out large-eddy simulations (LES), found error rates up to 100% between CFD and AAR, and similar discrepancies have been also reported by Schmidt *et al.* (2022). Such a large disagreement on a fundamental quantity of interest that is directly related to the integral of total losses does not appear fully compatible with the errors usually accepted for numerical simulations. This fact has been highlighted by Schillaci & Quadrio (2022), who systematically studied errors caused by lower-order numerical schemes, turbulence modelling or low spatial resolution in both LES and RANS simulations. The same conclusion was also reached by Johnsen (2024). One possible source of errors between RMM and CFD is the reconstruction of the geometry from CT scans, as discussed by Karbowski *et al.* (2023), but event this is not sufficient to justify the mismatch between with RMM and CFD.

In the present work, CFD results and the RMM measurement are compared for a silicone cast reconstructed from a CT scan. This is essential to remove several possible causes for disagreement, as e.g. the compliancy of the tissues, or the unavoidable changes of the anatomy between the moment the CT scan is taken and the execution of the RMM. Simulations of various fidelity levels are considered, to provide an indication

of the uncertainty that can be expected from CFD in terms of R. One source of systematic error, that is ultimately caused by the design of medical instruments, is also considered.

TEST CASE AND EXPERIMENTAL SETUP

The experimental setup is created to reproduce as closely as possible that of clinical exams, with the only distinction being that the cast is in scale 2:1 w.r.t. to the human anatomy. The cast is a preliminary version of that employed by Tauwald *et al.* (2024) for a tomo-PIV analysis of this flow; the 2:1 scale factor is meant to provide better optical access. In the AAR, the patient has one nostril sealed and breathes through a mask connected with the rhinomanometer. The rhinomanometer measures the flow rate directly with an inline flowmeter, together with two simultaneous pressure measurements. The first pressure is measured by a probe inserted in the sealing of the closed nostril: since the flow is at rest in the half of the nasal cavity corresponding to the closed nostril, this measure provides the pressure at the pharynx. The second pressure measurement is taken in the mask, to serve as a reference. This procedure is repeated for both sides of the nasal cavity, and the nasal resistance is then evaluated as the parallel of the left and right sides:

$$R_{\mathrm{tot},||} = \frac{R_{\mathrm{left}} R_{\mathrm{right}}}{R_{\mathrm{left}} + R_{\mathrm{right}}} \,. \tag{1}$$

One aspect that has received little attention in the literature is the location where the reference pressure measurement is taken. Rhinomanometers are connected to the mask via a socket that also hosts a filter. In many designs the reference pressure is not taken in the mask, but in this socket, just before the filter. In our experiment, two different locations for the reference pressure are considered (as explained in Fig. 1). The first location, in the socket before the filter, is denoted with F, and is most common in rhinomanometers. An alternative location is also considered, directly in the mask, and denoted by M. The pressure difference for the sealed nostril is then denoted with SN. With this notation, the nasal resistance can be measured in two ways:

$$R_F = \frac{P_{SN} - P_F}{Q} \quad \text{and} \quad R_M = \frac{P_{SN} - P_M}{Q} \,. \tag{2}$$

In the experiments, a volumetric pump is used to imposed the flow rate, which is measured by the rhinomanometer, while standard transducer are used for the pressure measurements.

The experimental data set created in this set includes both inhalation and exhalation, for the two configurations of left nostril or right nostril open; only inhalation is considered in this paper.

NUMERICAL METHODS

The employed DNS code is based on the one introduced by Luchini (2016), and is written in the CPL programming language (Luchini, 2020); it uses a finite-difference second-order discretization for the spatial derivatives of the incompressible Navier–Stokes equations together with an efficient immersed boundary method (IBM). The IBM corrects the solution to obtain vanishing values of the velocity interpolated at the boundary location. The correction is computed from the governing

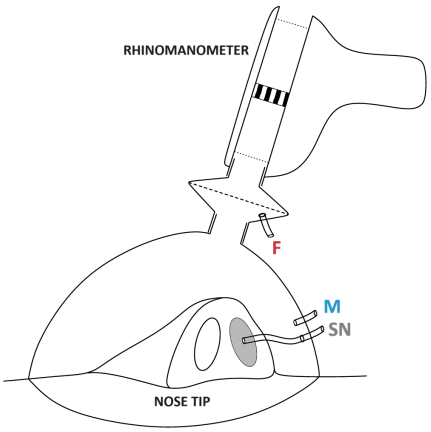

Figure 1. Sketch of measurement points in the experimental apparatus. The three locations of pressure probes are denoted with: sealed nostril (SN), corresponding to the pressure in the nasopharynx; before the filter (F), the typical choice in medical instruments; and at the mask (M).

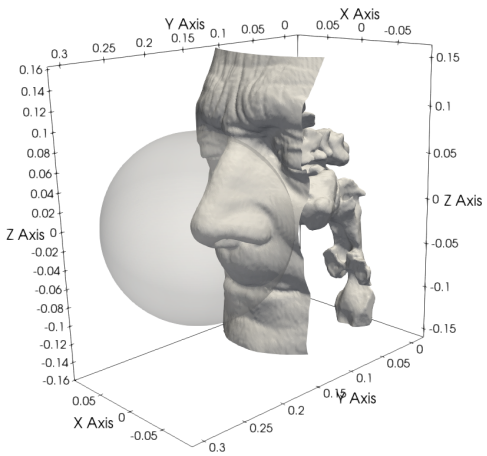

Figure 2. Geometry and computational domain in the simulations, including the sphere where inlet boundary conditions are imposed. Dimensions are in meters, the model has 2:1 geometrical scale.

equations specialized for the low Reynolds number regime, and only affects the grid points closest to the boundary. A prediction-correction method is employed, and the time integration is performed using a third-order Runge-Kutta scheme. The computational domain consists of a cuboid that encloses the model and a large sphere (approximately centred at the tip of the nose), which is used to enforce boundary conditions far from the nostrils (Fig. 2).

A constant pressure drop is set between the spherical inlet surface and the outlet, which is a horizontal cut of the trachea. To reproduce the AAR procedure, the patient-specific nasal geometry of the experiment is altered by sealing one nostril. The (temporally averaged) pressure difference necessary to estimate R is measured between the space included by the spherical inlet and the nostrils (corresponding to location M in the experiment), and the pressure behind the sealing of the sealed nostril (corresponding to location SN in the experiment). Lastly, it should be recalled that our setup is larger by a scale factor of 2 than the real patient; we work under the con-

straint of dynamical similarity. In the present work, we shall consider only results obtained for constant flow rates. A more realistic representation of the inhalation-exhalation cycle is not required for our aim, and it follows the set up of similar studies employing CFD to estimate the nasal resistance.

RANS simulations are carried out with the open-source software OpenFOAM, a set of C++ libraries for the numerical solution of partial differential equation on unstructured grids with the finite-volume method Weller *et al.* (1998). The OpenFOAM solver for incompressible steady-state cases is *simpleFoam*, which is based on the semi-implicit method for pressure-linked equations (SIMPLE). The turbulence model used for all simulations is the $k-\omega$ SST Menter *et al.* (2003), used in its standard formulation as implemented in the code. The grids for RANS simulations were created with the native utilities provided with the solver, *i.e.* with *blockMesh* (that is used to created an initial hexahedral structured grid), and *snappyHexMesh* (that adapts and refines the initial grid to the geometry).

The numerical data set created for the present study consists of: a) IBM simulations with increasingly higher spatial resolution (at identical driving pressure difference between inlet and outlet), to confirm that the code has the expected accuracy; b) a set of IBM simulations for the right nostril open, the left nostril open, and both nostrils open, each with a range of flow rates comparable with that in the experiments; here, two spatial resolutions are employed; c) RANS simulations for the left and right nostril open, for selected pressure differences, and three different resolution, including sets with both second-order and first-order numerical schemes for the coarsest grid.

RESULTS AND DISCUSSION

To provide an overview of the flow obtained with the time-resolved DNS simulations, the instantaneous velocity magnitude for a sagittal section of the nasal cavity is shown first in Fig. 3, together with the mean turbulent kinetic energy. Note that the considered geometry is not exactly symmetric, and the section shown here includes the turbinate regions of the right half but also roughly bisects the trachea – in case of perfect bi-lateral symmetry, the plane bisecting would correspond to the nasal septum that separates the two halves of the nasal cavity.

In the simulation considered here, both nostrils are open and the pressure difference between inlet and outlet is $\approx 6.13\,\mathrm{Pa}$, corresponding to a mean flow rate of approximately $630\,\mathrm{cm}^3/\mathrm{s}$, which are relatively high values w.r.t. the experiments. From the visualization, it is possible to appreciate that the passageways within the nasal cavity are thin enough to cause the flow to remain mostly laminar, at least for a relatively large range of flow rates. On the other hand, the flow becomes unsteady and possibly turbulent in the upper portion of the pharynx, where the respiratory tract is unified, and so it remains up to the outlet.

Accuracy of the IBM code

To verify that the IBM correction preserves the second-order accuracy of the spatial discretization, 10 simulations were carried out with a progressively higher resolution, for the same pressure difference between inlet and outlet of the case shown in Figure 3. The resolution spans from $\Delta x \approx 1\,\mathrm{mm}$, to $\Delta \approx 0.2\,\mathrm{mm}$, for which the number of grid points within the immersed boundary is $\approx 3.7\cdot 10^6$ and $\approx 0.47\cdot 10^9$, respectively. All simulations are carried out with a constant CFL number of 1.5.

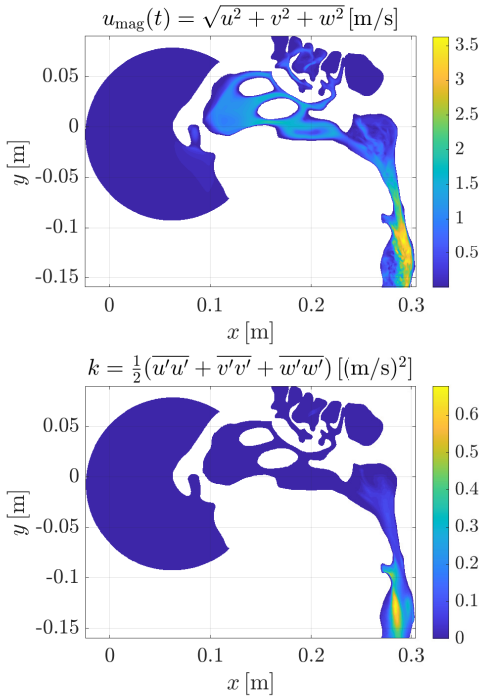

Figure 3. (top) Instantaneous velocity magnitude and (bottom) mean turbulent kinetic energy on a sagittal section of the computational domain in the IBM simulation with highest flow rate ($\overline{Q} \approx 630\,\mathrm{cm}^3/\mathrm{s}$).

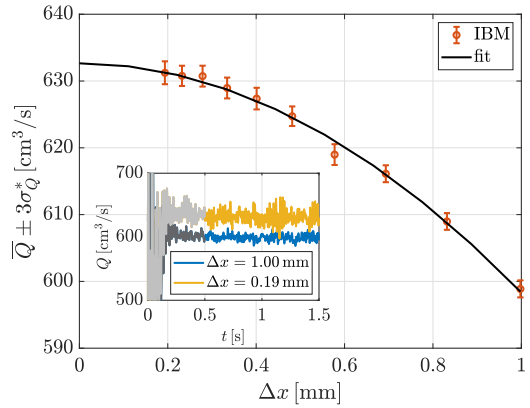

Figure 4. Order of accuracy of the IBM code. The time evolution of flow rates for the two simulations with finer and coarser resolutions is shown in the insert (grey denotes the initial transient before the average).

The flow observable chosen to verify the order of accuracy of the IBM is the time-averaged flow rate, denoted with $\overline{Q}$. The IBM simulations are carried out with the fluid at rest as initial condition, $\overline{Q}$ is sampled at the outlet for a period of $\Delta T = 1\mathrm{s}$ starting from $t = 0.5\mathrm{s}$, and an estimate of its variance, denoted by σ_Q, is obtained using the method proposed by Russo & Luchini (2017). The function $\overline{Q} = f(\Delta x)$ is fitted as: $f(\Delta x) = Q_0 + \alpha(\Delta x)^\beta$, where Q_0 and β are the asymptotic value of $\overline{Q}$ for $\Delta x \to 0$, and the order of accuracy, respectively. The values of these two parameter estimated with from fit are $Q_0 = 633\,\mathrm{cm}^3/\mathrm{s}$ and $\beta = 1.98$. The fitted curve is shown in Fig. 4 together with the quantity $\overline{Q} \pm 3\sigma^*_{\overline{Q}}$, demonstrating that the IBM implementation maintains the second-order accuracy

of the finite difference discretization. The same values are reported in Table 1, together with the relative error of $\overline{Q}$ w.r.t. the asymptotic value, Q_0. The relative error on the average flow rate is $\approx 1\%$ for $\Delta x \approx 0.5\,\text{mm}$, which is also a standard resolution for well executed CT scans.

Table 1. Data set used to verify the order of accuracy, including the relative error w.r.t to the asymptotic value Q_0. Bold font denotes the two resolutions considered hereafter in the comparison with RANS and experiments.

$\Delta x\,[\text{mm}]$	N_{points}	$\overline{Q} \pm 3\sigma^*_Q\,[\text{cm}^3/\text{s}]$	$(\overline{Q}-Q_0)/(\overline{Q}_0)$
1.00	$3.7 \cdot 10^6$	599.4 ± 1.3	5.7%
0.83	$6.3 \cdot 10^6$	608.8 ± 1.2	4.0%
0.69	$10.6 \cdot 10^6$	616.3 ± 1.3	2.8%
0.58	$18.0 \cdot 10^6$	619.9 ± 1.6	2.2%
0.48	$\mathbf{30.5 \cdot 10^6}$	$\mathbf{625.0 \pm 1.5}$	**1.3%**
0.40	$51.9 \cdot 10^6$	627.7 ± 1.6	0.9%
0.33	$\mathbf{92.0 \cdot 10^6}$	$\mathbf{629.8 \pm 1.6}$	**0.6%**
0.28	$157.8 \cdot 10^6$	631.3 ± 1.6	0.3%
0.23	$273.1 \cdot 10^6$	631.3 ± 1.5	0.3%
0.19	$471.8 \cdot 10^6$	632.2 ± 1.7	0.2%

The geometrical complexity of the anatomy and the chaotic – yet not entirely turbulent – nature of the flow make it difficult to use standard resolution indicators to assess whether the simulations carried out are fully-resolved DNS. For the purpose of the present paper, a resolution error of approximately 1% on $\overline{Q}$ is considered adequate and the two grids with $\Delta x = 0.48\,\text{mm}$ and $0.33\,\text{mm}$ are used later on for comparison with RANS results and experiments (for the finer one, only one flow rate is examined). For these two grids, the computational cost for a full run is approximately 100 and 500 CPU hours, respectively, which allows simulations without using dedicated HPC infrastructures.

RANS and IBM

The comparison between RANS and IBM simulations is carried out for similar flow rates to those in the experiment, in a range between 100 and $600\,\text{cm}^3/\text{s}$. The three grids for RANS have $0.67 \cdot 10^6$, $3.7 \cdot 10^6$, and $9.6 \cdot 10^6$ cells, thus ecompassing standard mesh sizes found in literature. All grids are made to satisfy the conventional mesh-quality requirements (*e.g.* on non-orthogonality and aspect ratio), but the first grid is quite coarser than that usually recommended for these simulations, the second is more similar to those employed for studies on the nasal cavity, and the third one is finer than average. Simulations for all the three grids are carried out using OpenFOAM built-in second order numerical schemes, which is of paramount importance Schillaci & Quadrio (2022). Furthermore, an additional set of simulations with the coarser grid used only first-order numerical schemes for the governing equations.

The quantities of interest considered now are the average flow rate, $\overline{Q}$, as defined before, and the average pressure difference between the inlet and a probe behind the sealing of the sealed nostril, denoted by $\overline{\Delta P} = \overline{P}_{SN} - \overline{P}_M$. These quantities, that are obtained from the time-averaged velocity and pressure fields, are analogous to the flow rate and pressure difference in the clinical/experimental measurements of R_M, and are shown in Fig. 5 for the right nostril (note that left and right are defined from the perspective of the doctor that is in front of patient taking the measurement).

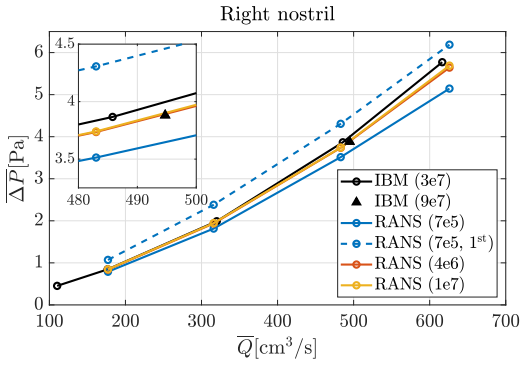

Figure 5. Pressure difference between the inlet and a probe behind the sealing of the sealed nostril as a function of the average flow rate for RANS and IBM simulations.

Overall, the agreement between RANS and IBM simulations is good, confirming the previous observation that using time-resolved simulations is not quite necessary to obtain a reasonable estimate of nasal resistance (at least, in the case of steady inflow). In particular, RANS simulations with mid and higher resolutions are in excellent agreement between each other for the entire range of flow rates and with the IBM simulations at lower resolution for flow rates below $\approx 400\,\text{cm}^3/\text{s}$. RANS are in better agreement with the higher-resolution IBM simulation at $Q \approx 490\,\text{cm}^3/\text{s}$, suggesting that the progressively worse mismatch between RANS and IBM simulations with low resolution is in fact caused by the stronger effect of low resolution in the latter ones. Grid-dependency effects on the RANS are apparent only for the coarse grid. In that case, simulations with second-order accuracy tend to underestimate dissipation, giving consistently lower $\overline{\Delta P}$. On the other hand, using first-order numerical scheme causes the opposite. These two competing effects keep the simulations that are supposed to be with the lowest fidelity level still similar enough to both the more accurate RANS and the time-resolved DNS simulations. Similar results, not shown here, were also obtained for the left nostril.

Simulations and experiments

Simulations data are now compared against experimental results, for both $\Delta P = P_{SN} - P_M$ and $P_{SN} - P_F$ and left and right nostrils (Fig. 6). Only IBM and RANS with coarse grid and second-order discretization are shown here, to provide a qualitative indication of the discrepancy between simulations with different fidelity level. The agreement between simulations and measurements of $P_{SN} - P_M$, which are supposed to be equivalent, is not excellent, in particular for the left nostril. The statistical errors on both simulations and experiment are negligible, and this lack of agreement indicates that there is a source of systematic error that has not been identified yet. Nevertheless, an even larger mismatch is found between the two experimental measurement series with reference pressure P_F and P_M. At all flow rates except the lowest one, the mismatch between $\Delta P = P_{SN} - P_M$ and $\Delta P = P_{SN} - P_F$ is also

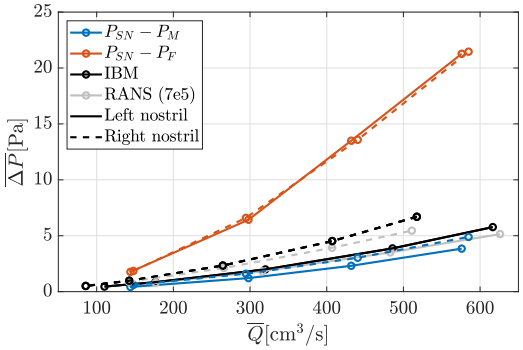

Figure 6. Comparison between experiments, including both $\Delta P = P_{SN} - P_M$ and $\Delta P = P_{SN} - P_F$ measurements, and $\Delta P = P_{SN} - P_M$ for the two simulations data sets with larger mismatch between each other.

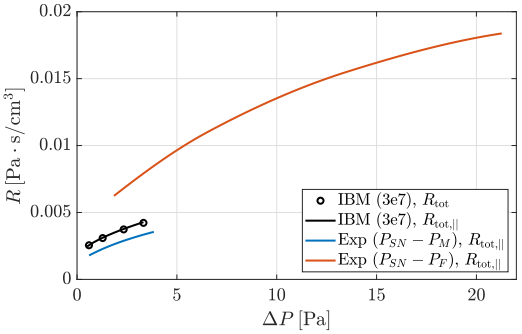

Figure 7. Comparison between nasal resistance from IBM simulations with both nostrils open and the total resistance computed for IBM simulations and experiments reproducing the rhinomanometry set up.

larger than that between RANS and IBM. Furthermore, both simulations and $P_{SN} - P_M$ measurements show that the two nostrils are not symmetric, the left nostril having a higher resistance than the right one (which is shown by lower $\overline{\Delta P}$ at the same $\overline{Q}$), while $P_{SN} - P_F$ measurements would indicate that the two nostrils are virtually identical.

To provide a more quantitative indication on how the sources of uncertainty considered so far affect the nasal resistance, R is evaluated for the two nostrils at the flow rates obtained for the IBM simulation with higher resolution, interpolating ΔP for the other data set (Tab. 2).

Table 2. Relative error on the resistance for both nostrils, using as reference simulation IBM (9e7), with $\overline{Q} \approx 414$ for the left nostril and ≈ 490 for the right nostril.

	Left	Right
$P_{SN} - P_M$ (Exp)	−39.9%	−24.5%
$P_{SN} - P_F$ (Exp)	168.0%	334.4%
IBM (3e7)	1.7%	2.6%
RANS0	−11.9%	−6.2%
RANS01st	5.5%	14.7%
RANS1	−2.4%	−0.01%
RANS2	−2.2%	0.01%

These results illustrate that the uncertainty related to the choice of reference pressure in the experiment is the largest one for both nostrils, by more than one order of magnitude for the right side. This mismatch is compatible with those reported in the literature between clinical measurements and CFD, whereas errors associated with all other sources of uncertainty are not large enough.

Total nasal resistance

Comparing the resistance for a single nostril has the same meaning both at fixed Q or fixed ΔP, as it would be for *e.g.* classical channel flows. The total nasal resistance in a rhinomanometry, however, is computed as the parallel of both nostrils and the expression $R_{\text{tot},||} = R_{\text{left}} R_{\text{right}} / (R_{\text{left}} + R_{\text{right}})$ holds at fixed ΔP – so that $R_{\text{tot},||}$ can only be computed for a value of ΔP for which both R_{left} and R_{left} are known. It follows that a discrepancy in ΔP modifies the value of $R_{\text{tot},||}$ as well as the interval where it is defined. CFD of course allows a more direct evaluation of the nasal resistance, which can be measured from simulations of the nasal cavity with both nostrils open. The nasal resistance evaluated directly in this way is denoted with R_{tot} hereafter. Fig. 7 shows the nasal resistance evaluated directly from the IBM simulations with coarser grid and both nostril open, and that computed as parallel of right and left nostrils for the simulations and experiments that have been discussed in the previous section. Note that interpolated values of $\Delta P = f(\overline{Q})$ are used to compute R when necessary. The relative error between $R_{\text{tot},||}$ and R_{tot} is reported in Tab. 3) for the highest ΔP for which it is possible to have a comparison among all data sets. The $R_{\text{tot},||}$ and R_{tot} computed from simulations are in good agreement, as assumed in a rhinomanometry. This is not necessary a trivial result, given the anatomical complexity of upper portion of the pharynx and the inevitable alteration of the flow caused by sealing one nostril at the time. Similarly to the results for a single nostril, experimental measurements using the standard reference pressure, P_F, overestimate R, while those with the alternative reference pressure measurement, P_M, underestimate it. The discrepancy is apparently smaller in this case than that reported in the single-nostril comparison, because the definition of $R_{\text{tot},||}$ causes a shift towards the right when ΔP is systematically increased. In particular, the comparison is now carried out between a regime with high flow rates for the two data sets with consistently lower ΔP and a regime with low flow rates the for data set with consistently higher ΔP. Nonetheless, it is confirmed that the defini-

Table 3. Relative error on the total nasal resistance computed as $R_{\text{tot},||}$, using as reference R_{tot} from the simulation IBM (3e7) with both nostrils open and $\Delta P = 3.22$ Pa.

	$(R_{\text{tot},||} - R_{\text{tot}})/R_{\text{tot}}$
IBM (3e7)	1.2%
Exp ($P_{SN} - P_M$)	−20.9%
Exp ($P_{SN} - P_F$)	87.4%

tion of reference pressure as P_F in the rhinomanometry, *i.e.* not directly in the mask but further downstream along the flow, can cause a systematic bias compatible with the mismatch reported in the literature between CFD and clinical measurements of nasal resistance.

CONCLUSIONS

A finite-difference code with a new immersed boundary method has been presented, showing a 2^{nd}-order accuracy in time-resolved simulations of complex geometries. This code allows to carry out well-resolved simulations of the flow in the nasal cavity with a computational cost low enough for a workstation or even a high-end personal computer.

A new data set to describe the flow in the nasal cavity was created, including simulations with the IBM code, RANS, and experimental results, reproducing of a standard medical exam. While carrying out fully-resolved DNS at all considered flow rates was out of the scope of the present work, the data set allowed to examine multiple sources of error in the evaluation of the nasal resistance. It was found that the only source of uncertainty large enough to account for the mismatch between CFD and clinical exams consistently reported in the literature is the measurement location of reference pressure in the experiment. The fact that intrinsic uncertainty of CFD are not low enough to account for the discrepancy is in agreement with what reported in previous work and with the prevalence of laminar flow is most in the region of interest, in particular for the steady boundary conditions often used in these simulations.

Rhinomanometers tend to share common elements in their design, in particular the fact that the reference pressure is located relatively far from the nostrils, but the fact that only one instrument was considered remains a limitation of the present study. A broader set of conditions, including full respiration cycles, should be considered as well to provide a more precise description of numerical errors.

ACKNOWLEDGMENTS

This research has been partially supported by ICSC–Centro Nazionale di Ricerca in High Performance Computing, Big Data, and Quantum Computing funded by European Union—NextGenerationEU. MQ acknowledges support from the PRIN 2022 project, cod.2022BYA5AF CUP D53D2300343006. Computing time was provided by the CINECA Italian Supercomputing Center through the ISCRA-B projects ONOSE-AN and ONOSE-AI.

REFERENCES

Berger, M., Giotakis, A.I., Pillei, M., Mehrle, A., Kraxner, M., Kral, F., Recheis, W., Riechelmann, H. & Freysinger, W. 2021 Agreement between rhinomanometry and computed tomography-based computational fluid dynamics. *Int J CARS* **16**, 629–638.

Calmet, H., Inthavong, K., Owen, H., Dosimont, D., Lehmkuhl, O., Houzeaux, G. & Vázquez, M. 2021 Computational modelling of nasal respiratory flow. *Computer Methods in Biomechanics and Biomedical Engineering* **24** (4), 440–458.

Johnsen, Sverre Gullikstad 2024 Computational Rhinology: Unraveling Discrepancies between In Silico and In Vivo Nasal Airflow Assessments for Enhanced Clinical Decision Support. *Bioengineering* **11** (3), 239.

Karbowski, K., Kopiczak, B., Chrzan, R., Gawlik, J. & Szaleniec, J. 2023 Accuracy of virtual rhinomanometry. *Polish Journal of Medical Physics and Engineering* **29** (1), 59–72.

Kimbell, J.S., Garcia, G.J.M., Frank, D.O., Cannon, D.E., Pawar, S.S. & Rhee, J.S. 2012 Computed nasal resistance compared with patient-reported symptoms in surgically treated nasal airway passages: A preliminary report. *Am. J. Rhinology \& Allergy* **26** (3), e94–e98.

Luchini, P. 2016 Immersed-boundary simulation of turbulent flow past a sinusoidally undulated river bottom. *Eur. J. Mech. B / Fluids* **55**, 340–347.

Luchini, P. 2020 CPL. Available at https://CPLcode.net.

Menter, F.R., Kuntz, M. & Langtry, R. 2003 Ten Years of Industrial Experience with the SST Turbulence Model. *Turbulence, Heat and Mass Tansfer* **4**, 8.

Osman, J., Großmann, F., Brosien, K., Kertzscher, U., Goubergrits, L. & Hildebrandt, T. 2016 Assessment of nasal resistance using computational fluid dynamics. *Current Directions in Biomedical Engineering* **2** (1), 617–621.

Quadrio, M., Pipolo, C., Corti, S., Lenzi, R., Messina, F., Pesci, C. & Felisati, G. 2014 Review of computational fluid dynamics in the assessment of nasal air flow and analysis of its limitations. *Eur Arch Otorhinolaryngol* **271** (9), 2349–2354.

Radulesco, T., Meister, L., Bouchet, G., Giordano, J., Dessi, P., Perrier, P. & Michel, J. 2019 Functional relevance of computational fluid dynamics in the field of nasal obstruction: A literature review. *Clin. Otolaryngol.* **44** (5), 801–809.

Rhee, J.S., Book, D.T., Burzynski, M. & Smith, T.L. 2003 Quality of Life Assessment in Nasal Airway Obstruction. *The Laryngoscope* **113** (7), 1118–1122.

Russo, S. & Luchini, P. 2017 A fast algorithm for the estimation of statistical error in DNS (or experimental) time averages. *J. Comput. Phys.* **347**, 328–340.

Schillaci, A., Boracchi, G., Pipolo, C. & Quadrio, M. 2022 A CFD-augmented machine-learning approach for the classification of nasal pathologies. In *EUROMECH Fluid Mechanics Conference*. Athens (Greece).

Schillaci, A., Hasegawa, K., Pipolo, C., Boracchi, G. & Quadrio, M. 2024 Comparing flow-based and anatomy-based features in the data-driven study of nasal pathologies. *Flow* **(in press)**.

Schillaci, A. & Quadrio, M. 2022 Importance of the numerical schemes in the CFD of the human nose. *Journal of Biomechanics* **138**, 111100.

Schmidt, N., Behrbohm, H., Goubergrits, L., Hildebrandt, T. & Brüning, J. 2022 Comparison of rhinomanometric and computational fluid dynamic assessment of nasal resistance with respect to measurement accuracy. *Int J CARS* .

Tauwald, S.M., Erzinger, F., Quadrio, M., Rütten, M., Stemmer, C. & Krenkel, L. 2024 Tomo-PIV in a patient-specific model of human nasal cavities: A methodological approach. *Meas. Sci. Technol.* **35** (5), 055203.

Vogt, K., Jalowayski, A.A., Althaus, W., Cao, C., Han, D. M., Hasse, W., Hoffrichter, H., Mösges, R., Pallanch, J.F., Shah-Hosseini, K., Peksis, K., Wernecke, K., Zhang, L. T. & Zaporoshenko, P. 2010 4-Phase-Rhinomanometry (4PR)–basics and practice 2010. *Rhinology. Supplement* **21**, 1–50.

Weller, H.G., Tabor, G., Jasak, H. & Fureby, C. 1998 A Tensorial Approach to Computational Continuum Mechanics using Object-Oriented Techniques,. *Computers in Physics* **12** (6), 620–631.